



# Human serum albumin gradient in serous ovarian cancer cryosections measured by fluorescence lifetime

FANGRUI LIN,<sup>1</sup> CHENSHUANG ZHANG,<sup>1</sup> YANPING LI,<sup>1</sup> JUNSHUAI YAN,<sup>1</sup> YUNJIAN XU,<sup>1</sup> YING PAN,<sup>2</sup> RUI HU,<sup>1</sup> LIWEI LIU,<sup>1,3</sup> AND JUNLE QU<sup>1,4</sup>

<sup>1</sup>Key Laboratory of Optoelectronic Devices and Systems of Guangdong Province & Ministry of Education, College of Physics and Optoelectronic Engineering, Shenzhen University, Shenzhen, Guangdong Province 518060, China

<sup>2</sup>China–Japan Union Hospital of Jilin University, Changchun, China

<sup>3</sup>liulw@szu.edu.cn

<sup>4</sup>jlqu@szu.edu.cn

**Abstract:** Human serum albumin (HSA) is a depot and carrier for many endogenous and exogenous molecules in blood. Many studies have demonstrated that the transport of HSA in tumor microenvironments contributes to tumor development and progression. In this report, we set up a multimodal nonlinear optical microscope system, combining two-photon excitation fluorescence, second harmonic generation, and two-photon fluorescence lifetime imaging microscopy. The fluorescence lifetime of a small squaraine dye (SD) is used to evaluate HSA concentrations in tumor tissue based on specific binding between SD and HSA. We used SD to stain the cryosections from serous ovarian cancer patients in high-grade (HGSOC) and low-grade (LGSOC), respectively, and found a gradient descent of HSA concentration from normal connective tissue to extracellular matrix to tumor masses from 13 to 2  $\mu\text{M}$  for LGSOC patients and from 36 to 12  $\mu\text{M}$  for HGSOC patients. We demonstrated that multimodal nonlinear optical microscopy can obtain similar results as those from traditional histologic staining, thus it is expected to move to clinical applications.

© 2021 Optical Society of America under the terms of the [OSA Open Access Publishing Agreement](#)

## 1. Introduction

The tumor microenvironment, which contains extracellular matrix (ECM) proteins and the vasculature, plays a vital role in supporting tumor progression and ultimately the initial stages of metastasis [1–3]. As the most abundant protein in plasma, human serum albumin (HSA) provides the physiological functions in the regulation of capillary membrane permeability and ligand binding and transport [4,5]. Meanwhile, HSA has been considered as the main energy and nutrition source for tumor growth, resulting in a higher HSA level is distributed around solid tumors [6–9]. Therefore, HSA has been extensively used in controlled release systems as versatile vehicles for the delivery of anticancer drugs to local tumors [10–12]. Shinichi Ohno et al. reported on the distribution of serum albumin (SA) in the xenografted mouse model qualitatively using immunohistochemical staining and cryotechnique, demonstrating that SA is predominantly distributed in the tumor blood vessels and in the connective tissues around tumor masses [13]. However, the concentration distribution of HSA in human solid tumors is still lack of understanding, which is associated with tumor behavior in vivo, including development, progression, and metastasis [9].

Two-photon fluorescence lifetime imaging microscopy (TP-FLIM) is a powerful technology to visualize the distribution of fluorophores' excited state lifetimes which are associated with a molecule's chemical environment or binding state [14]. In the past decade, TP-FLIM has been

used to visualize the distribution of anticancer drug [15] and ion concentrations [16] in the tumor microenvironment, and also to distinguish skin disease [17] and cancer grades [18]. Combined with other nonlinear optical microscopic imaging, including two-photon excitation fluorescence (TPEF) and second harmonic generation (SHG), a multimodal nonlinear optical microscope system has emerged as a potential tool for assisting conventional histology to discriminate the tumor cells in tissue by supplying additional information about the protein content and collagen fiber orientation in the tumor microenvironment [19].

Recently, we reported that the fluorescence lifetime of a small squaraine dye (SD) with large two-photon absorption cross-sections can selectively respond to the bovine SA concentration in the solution and cultured ovarian cancer cells [20,21]. In this study, we set up a multimodal nonlinear optical microscope system, including TPEF, SHG, and TP-FLIM modules. Furthermore, we identified the specificity of SD to HSA and used SD to stain the cryosections of carcinomas' outer margins from serous ovarian cancer patients at high-grade (HGSOC) and low-grade (LGSOC), respectively. With the calibration in solutions based on phasor-plot, our results exhibited a significant gradient decrease in the HSA concentration from connective tissue to the ECM to tumor cells. Compared with conventional histological staining, our method can provide a rapid and quantitative analysis of HSA concentration in the tumor microenvironment, and can also distinguish tumor masses from surrounding normal tissue, which has great potential to assist clinical cryobiopsy.

## 2. Materials and methods

### 2.1. Reagents

The synthesis of SD was described in our previous report [21]. HSA, hemoglobin, transferrin, myoglobin, collagen, fibronectin, laminin, elastin, and proteoglycan were purchased from Sigma-Aldrich Co. (St. Louis, MO, USA) and dissolved in phosphate-buffered saline (PBS) as 1 mM mother liquors for subsequent use.

### 2.2. Preparation of cryosections and staining

The ovarian cancer tissue samples used in this study were obtained from the China–Japan Union Hospital of Jilin University. According to the International Federation of Gynecology and Obstetrics and TNM classification standards, experienced gynecological oncologists conducted classification and histological identification. After surgery, the outer marginal tissues of ovarian carcinomas were immersed in optimal cutting temperature compound immediately. Then, 5  $\mu$ m thick serial cryosections were obtained by freezing microtome (CM1850, Leica, Germany) and stored at -20 °C for subsequent staining.

The sections were fixed in acetone for 1 min and immersed in PBS for 1 min rehydration. Then, 40  $\mu$ M SD was used to stain the sections for 2 min at room temperature (RT). After three washes in PBS, the sections were ready for subsequent microexamination. H&E staining was used to assess pathological contrasts. IHC staining of HSA (IHC–HSA) was routinely conducted following the process reported previously [22,23]. The sections were first blocked with 1% hydrogen peroxide in PBS and incubated in PBS with 5% fish gelatin (G7765, Sigma-Aldrich, USA) for 1 h. They were treated with rabbit polyclonal anti-HSA antibody (PA5-85166, Invitrogen, Norway) overnight at 4 °C, and were incubated in biotinylated goat anti-rabbit IgG antibody (A0277, Beyotime, China) for 1 h at RT. The diaminobenzidine horseradish peroxidase color development kit (P0203, Beyotime, China) was used to visualize the immunoreaction products.

### 2.3. Multimodal nonlinear optical microscope system

Figure 1 shows a laser scanning microscope (A1RMP+, Nikon, Japan) equipped with an ultrashort (100 fs pulse width) pulsed mode-locked 80 MHz titanium sapphire laser with a tunable

wavelength from 700 to 1,300 nm (Chameleon Discovery, Coherent, USA) as the excitation source. Two high-sensitive GaAsP photomultipliers (PMT) are coupled in the non-descanned light path as detectors for TPEF and SHG imaging. By synchronously connecting with the laser source and scanner, the TP-FLIM module containing a high-speed time-resolved PMT (HPM-100-40, Becker & Hickl, Germany) and time-correlated single-photon counting (TCSPC) module (SPC-150/DCC-100, Becker & Hickl, Germany) is also incorporated into the non-descanned light path and switched with a flip mirror. For measuring the emission spectra of samples under two-photon excitation, a portable fiber-spectrometer (QEpro, Ocean Optics, USA) is mounted on the descanned port of the microscope. The 720 nm (FF01-720/SP, Semrock, USA) short-pass filters (SPF) were set in the emission path as IR-cut filters. Excitation/emission and TPEF/SHG signals were separated using the 735 nm (FF735-Di02, Semrock, USA) and 605 nm (FF605-Di02, Semrock, USA) dichroic mirror (DM), respectively. Two 655/40 nm (FF02-655/40, Semrock, USA) band-pass filters (BPF) are used to collect the fluorescence of SD for TPEF and TP-FLIM. A 420/10 nm (FF01-420/10, Semrock, USA) BPF is used to selectively detect the SHG signal with 840 nm excitation. The images were obtained by 2× and 10× objectives (CFI Plan Apo λ 2x/10x, Nikon, Japan), respectively. The average power at the sample surface was approximately 1 mW for TPEF and TP-FLIM imaging, and was approximately 14 mW for SHG imaging (measured by PM130D, Thorlabs, USA).

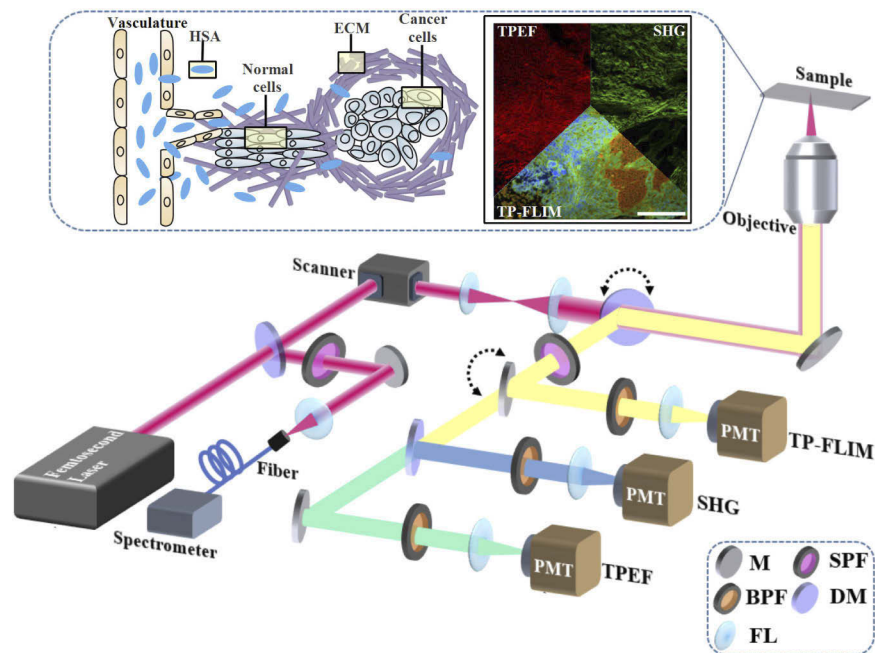


**Fig. 1.** A schematic of multimodal nonlinear optical microscope system. M: mirror; SPF: short-pass filter; BPF: band-pass filter; DM: dichroic mirror; FL: focal lens. Two dotted arcs represent the switchable light path. Insert: the transport process of HSA from the vasculature to connective tissue to tumor mass (left); visualization of HSA concentration in tumor microenvironment with multimodal nonlinear microscopy (right). Scale bar: 150 μm.

#### 2.4. Phasor-plot analysis

For TP-FLIM imaging, SPCM acquisition software (v.9.83, Becker & Hickl, Germany) was used in first-in-first-out (FIFO) mode where photon arrival times were recorded relative to pixel clocks from the scanner and excitation pulses from the laser. Jameson et al. introduced a phasor-plot

graphically representing the mathematics to resolve heterogeneous systems [24]. For the TCSPC technique, the decay data from each pixel of an image are transformed to the Fourier space using:

$$s_{ij}(\omega) = \int_0^\infty I(t) \sin(n\omega t) dt / \int_0^\infty I(t) dt, \quad (1)$$

and

$$g_{ij}(\omega) = \int_0^\infty I(t) \cos(n\omega t) dt / \int_0^\infty I(t) dt, \quad (2)$$

where  $i$  and  $j$  represent the pixel of the image, sine ( $s$ ) and cosine ( $g$ ) are phasor coordinates,  $\omega = 2\pi f$  ( $f$  is the laser repetition rate), and  $n$  is the harmonic frequency. The in-house written codes running on MATLAB (MathWorks, USA) were used to analyse FLIM phasor data. Independent from their location in the FLIM image, pixels with similar decay signatures form clusters in the phasor-plot.

### 3. Results and discussion

#### 3.1. Calibration of HSA concentration in solutions based on the fluorescence lifetime of SD

First, we evaluated the specificity of SD to HSA by investigating the absorption and fluorescence emission spectra of SD in PBS by adding HSA and different proteins existing in tissue generally. The results indicated that SD molecules bound with HSA specifically because of hydrophobic and electrostatic interactions (Fig. S1).

Conventional detection of proteins based on fluorescence intensity is usually qualitative or semiquantitative, because fluorescence intensity signals are strongly affected by multifarious environmental influences including fluctuations of light source power and voltage gain, autofluorescence of tissues, and concentration of probes. Here, in consideration of a great advantage of phasor-plot-based TP-FLIM, an inherent ability to distinguish the discrepant physicochemical microenvironment around fluorescent probes, which is fluorescence intensity-independent, we used TP-FLIM to measure the relative concentration of endogenic HSA in cryosections quantitatively. The main challenge is the calibration of the fluorescence lifetime of the SD response to HSA inside the slides. Like ion concentration imaging in tissue based on phasor-plot analysis [16], we measured the calibration curve of the fraction of the SD molecules bound to HSA ( $F_b$ ) response to HSA concentrations in solutions under physiological conditions (PBS buffer; pH 7.0) using Hill's dynamical model. SD samples with known HSA concentrations ( $[HSA]$ ) were loaded in capillary sampling tubes to implement TPEF and TP-FLIM measurements. Figure 2(A) shows that the free (red circle) and HSA-bound (blue circle) forms of SD have different fluorescence intensity and fluorescence lifetime, which can be separated in the phasor-plot and identified by  $R_f$  (red line) and  $R_b$  (blue line), respectively. The corresponding two-photon emission spectra of regions of interest (ROI) are shown in Fig. S2. All clusters are linearly distributed in the phasor-plot, indicating that any cluster represented by a phasor  $R$  (black line) is a combination of two distinct species  $R_f$  and  $R_b$  weighted by the relative fluorescence intensity of the free ( $\varepsilon_f$ ) and bound ( $\varepsilon_b$ ) states and concentrations of the free ( $[SD]$ ) and bound ( $[HSA-SD]$ ) SD molecules. The corresponding ratio is given by [16]:

$$\frac{[HSA-SD]}{[SD]} = \frac{\varepsilon_f}{\varepsilon_b} \cdot \frac{||\vec{R_f} - \vec{R}||}{||\vec{R} - \vec{R_b}||}. \quad (3)$$

For an equilibrated system, the equilibrium constant is given as follows:

$$K_D = [HSA][SD]/[HSA-SD]. \quad (4)$$

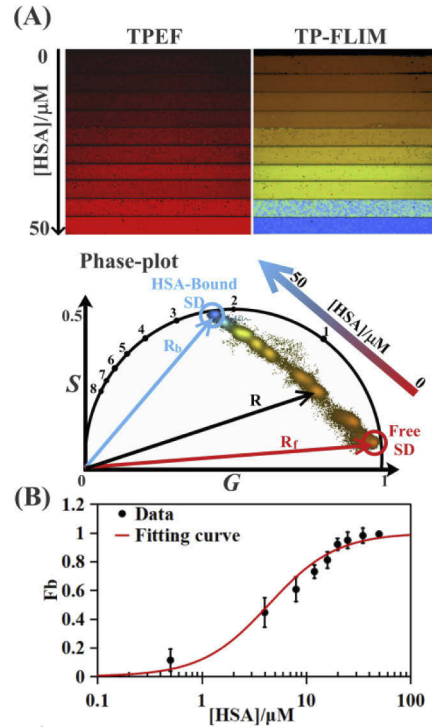


**Fig. 2.** Calibration of HSA concentration in solution. (A) TPEF imaging of the SD solution containing various HSA concentrations was obtained by 2× objective with 840 nm excitation. The pseudo-color lifetime image and corresponding phasor-plot were obtained by TP-FLIM. The red (0 μM) and blue (50 μM) circles indicate the free and HSA-bound SD species, respectively. (B) The corresponding  $F_b$  calculated from the phasor distributions at different HSA concentrations in (A). The results were obtained from three independent experiments. The calibration curve was fitted with a Hill's model (red line), and returned a  $K_D = 4.26$  μM.

$F_b$  can be calculated using the following equation:

$$F_b = [HSA - SD] / ([HSA - SD] + [SD])$$

$$= \frac{\varepsilon_f \frac{||\vec{R_f} - \vec{R}||}{||\vec{R} - \vec{R_b}||}}{1 + \frac{\varepsilon_f \frac{||\vec{R_f} - \vec{R}||}{||\vec{R} - \vec{R_b}||}}{\varepsilon_b \frac{||\vec{R_f} - \vec{R}||}{||\vec{R} - \vec{R_b}||}}}. \quad (5)$$

Finally, [HSA] can be calculated as follows:

$$[HSA] = \frac{K_D F_b}{1 - F_b}. \quad (6)$$

In the solution with the known [HSA], Fig. 2(B) shows the corresponding  $F_b$  calculated using Eq. (5) (black solid circle) and the curve fitted by a Hill's function (red line), resulting in the value of  $K_D$  (4.26 μM) used for subsequent measurements of [HSA] in cryosections.

### 3.2. Quantitative analysis of [HSA] in ovarian cancer patients' cryosections

As a main nutrition source during growth and metastasis of tumor cells, the concentration of HSA inside tumors is a valuable information in the tumor microenvironment for assisting the clinical diagnosis and therapy. Three sequential cryosections of an LGSOC patient were



stained with H&E, SD, and IHC-HSA, respectively. In Fig. 3(A), the red dashed line shows the boundary of tumor cells (TC, red circle), in which round and heterotypic nuclei are crowded and hyperchromatic, and normal connective tissue (CT, green square). TPEF imaging of SD exhibits a different brightness [Fig. 3(B)], indicating that [HSA] is discrepant across the tissue. The SHG signal is attenuated markedly in the TC area [Figs. 3(C and D), white arrows]; this can be attributed to the degradation of collagen near tumor masses by abnormal matrix metalloproteinase generation [25]. The TPEF of SD and SHG signals were confirmed by measuring the emission spectral of ROI [Fig. S3(B)]. Figures 3(E–I) show the phase-plot analysis of TP-FLIM visualizing a descending [HSA] in spatial distribution by highlighting the pixels with three [HSA] ranges (9–15  $\mu\text{M}$  in blue, 3–9  $\mu\text{M}$  in green, and 1–3  $\mu\text{M}$  in red), which exactly partitioned the area of CT, extracellular matrix (ECM) of tumor masses, and TC. The corresponding fluorescence lifetime intervals were shown in Table S1. The photograph of IHC-HSA [Fig. 3(J)] shows a similar distribution of HSA, in which positive IHC staining exists in CT and ECM principally, confirming the results obtained from TP-FLIM.

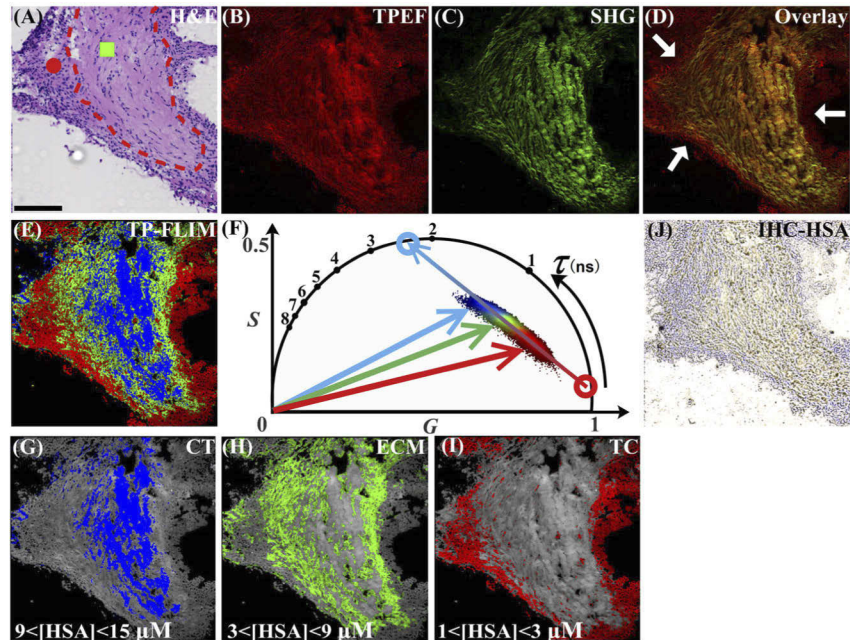


**Fig. 3.** Quantitative analysis of [HSA] in the cryosection of an LGSOC patient. (A) H&E imaging; TC (red solid circle) and CT (green solid square) area were differentiated by a red dashed line; Scale bar: 150  $\mu\text{m}$ ; (B) TPEF imaging under 840 nm excitation; (C) SHG imaging; (D) Overlay of TPEF and SHG; (E) Pseudo-color fluorescence lifetime imaging; Pixels were highlighted with three colors by selecting phasors with the same color in the corresponding phasor-plot (F); (G–I) CT, ECM, and TC areas with three serial [HSA] gradients were presented separately from (E); (J) IHC-HSA imaging.

The  $K_d$  value in tumors should be approximated in the physiological buffer solution because known [HSA] are unobtainable in human tissue. Because of the strong fluorescence of SD under 840 nm excitation, the autofluorescence of endogenous fluorophores in ovarian carcinomatous tissue, such as nicotinamide adenine dinucleotide and flavin adenine dinucleotide [26,27], was undetectable with the excitation power used in experiments, which can be confirmed from the TPEF images and emission spectra of the samples unstained with SD [Fig. S3(A)]. Therefore, the phase-plot of tissue samples shows the same  $R_f$  and  $R_b$  as those in the solution [Figs. 2(A)

and 3(F)]. These results demonstrated that the fluorescence lifetime of SD molecules could be used to analyze HSA levels in tumor cryosections quantitatively and rapidly (staining process within 5 min). Using the inherent ability of the phasor-plot approach to image segmentation, the [HSA] gradient was presented from CT to ECM to TC. Together with TPEF and SHG imaging, multimodal nonlinear optical microscopy visualized the tumor microenvironment, including the distribution of tumor masses, [HSA], and collagen, providing more physiological information to assist clinical cryobiopsy.

Next, we implemented the same measurements of the samples from an HGSOc patient (Fig. 4). As shown in Figs. 4(A–E), because of the high invasiveness of HGSOc, TC infiltrated the CT area, decreasing the SHG signal in CT (white arrows). However, the corresponding phasors [Fig. 4(F)] are disparate as those in LGSOc [Fig. 3(F)], resulting in three higher [HSA] levels: 23–44  $\mu\text{M}$  in blue, 14–23  $\mu\text{M}$  in green, and 5–14  $\mu\text{M}$  in red [Figs. 4(G–I)]. IHC–HSA confirmed a similar [HSA] gradient decline from CT to TC [Fig. 4(J)]. Figure 5 shows the statistical results of [HSA] in the CT, ECM, and TC areas from LGSOc (from 13 to 2  $\mu\text{M}$ , 9 samples) and HGSOc (from 36 to 12  $\mu\text{M}$ , 12 samples) patients, respectively. In reality, SHG imaging was used to visualize the distribution of collagen in tissue, and the significantly weaker SHG signal of degenerated collagen helps us to distinguish the tumor tissue from the normal tissue in the cryosections. TP-FLIM imaging was used to quantify [HSA] levels in different regions of the cryosections. Combining each type of nonlinear imaging assay, our method provided a rapid and quantitative analysis of [HSA] levels in the tumor microenvironment, and demonstrated a

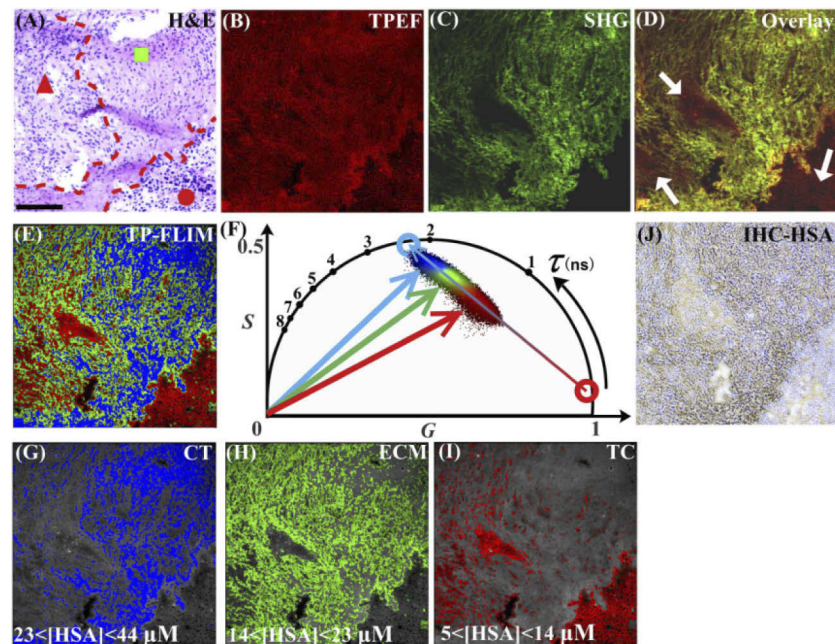


**Fig. 4.** Quantitative analysis of [HSA] in the cryosection of an HGSOc patient. (A) H&E imaging; The red solid circle represents the TC area; the green solid square represents the CT area; the red solid triangle represents the infiltration of TC into the surrounding CT area; Scale bar: 150  $\mu\text{m}$ ; (B) TPEF imaging under 840 nm excitation; (C) SHG imaging; (D) Overlay of TPEF and SHG; (E) Pseudo-color fluorescence lifetime imaging; Pixels were highlighted with three colors by selecting phasors with the same color in the corresponding phasor-plot (F); (G–I) CT, ECM, and TC areas with three serial [HSA] gradients were presented separately from (E); (J) IHC–HSA imaging.

gradient descent of [HSA] from a normal tissue to a tumor tissue. Higher [HSA] levels were found inside solid tumors of HGSOC patients, which could be attributed to increased permeability of the microvasculature for HGSOC, allowing an increased HSA accumulation in the tumor microenvironment [28,29]. Although the whole tumors usually become highly vascularized by angiogenesis [30], there are some blood vessels and blood capillaries in tumor masses that were not functional for transporting serum albumin [13,31], which may be attributed to the decreased intravascular pressure and collagen matrix content, hypoxic environment, and abnormal vascular morphology [31–33]. In addition, the discrepant molecular structure of blood vessels was also partly associated with the lower permeability of blood vessels in tumor mass than that in the surrounding connective tissue [31,34], which locally disturbed the blood circulation and resulted in lower [HSA] levels in tumor mass regions. These results show that different HSA levels could offer additional information for diagnosing grades of SOC and suggest that drugs loaded in HSA would assemble better in solid tumors for HGSOC. On the other side, the gradual decrease in [HSA] from CT to TC visualized the process of HSA transport in SOC (Insert in Fig. 1), which were similar to those found in the xenografted mouse model [13,31], demonstrating that endogenous HSA is predominantly distributed in collagenous stroma around tumor masses rather than in their internal areas.

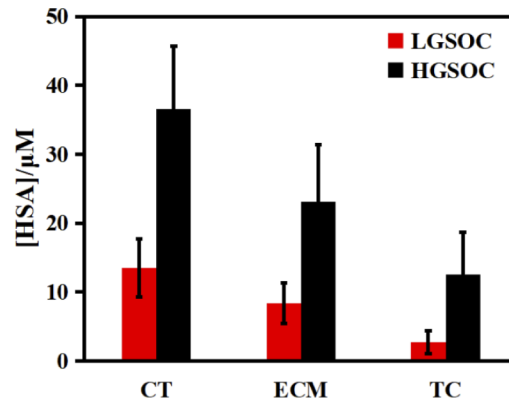


**Fig. 5.** Statistical results of [HSA] in different compartments of tissues from LGSOC (9 samples) and HGSOC (12 samples) patients.

#### 4. Conclusion

We present a novel method to visualize the microenvironment of SOC tissue using the multimodal nonlinear optical microscopy. With specific responses of the SD fluorescence lifetime to HSA, we found a gradient decrease in HSA concentrations from CT to TC inside solid tumors for both LGSOC and HGSOC patients, whereas higher HSA levels existed in HGSOC patients. Our method presents a rapid and quantitative analysis of the distribution of HSA concentrations and tumor masses, exhibiting similar results to conventional histological staining, thus demonstrating that multimodal nonlinear optical microscopy could assist clinical diagnosis, especially for cryobiopsy during tumor resection.

**Funding.** National Natural Science Foundation of China (61525503, 61620106016, 61722508, 61935012, 61961136005); (Key) Project of Department of Education of Guangdong Province (2016KCXTD007); Shenzhen Science and Technology Funding (JCYJ20180305124902165).

**Disclosures.** The authors declare no conflicts of interest.

**Supplemental document.** See [Supplement 1](#) for supporting content.



## References

1. E. Sahai, "Illuminating the metastatic process," *Nat. Rev. Cancer* **7**(10), 737–749 (2007).
2. A. Orimo, P. B. Gupta, D. C. Sgroi, F. Arenzana-Seisdedos, T. Delaunay, R. Naeem, V. J. Carey, A. L. Richardson, and R. A. Weinberg, "Stromal fibroblasts present in invasive human breast carcinomas promote tumor growth and angiogenesis through elevated SDF-1/CXCL12 secretion," *Cell* **121**(3), 335–348 (2005).
3. J. Condeelis, R. H. Singer, and J. E. Segall, "The great escape: when cancer cells hijack the genes for chemotaxis and motility," *Annu. Rev. Cell Dev. Biol.* **21**(1), 695–718 (2005).
4. T. W. Evans, "Review article: albumin as a drug—biological effects of albumin unrelated to oncotic pressure," *Aliment. Pharm. Ther.* **16**, 6–11 (2002).
5. C. M. Mendez, C. J. McClain, and L. S. Marsano, "Albumin therapy in clinical practice," *Nutr. Clin. Pract.* **20**(3), 314–320 (2005).
6. F. Kratz, "Albumin as a drug carrier: design of prodrugs, drug conjugates and nanoparticles," *J. Controlled Release* **132**(3), 171–183 (2008).
7. D. Fukumura and R. K. Jain, "Tumor microvasculature and microenvironment: targets for anti-angiogenesis and normalization," *Microvasc. Res.* **74**(2–3), 72–84 (2007).
8. M. Yang, S. Hoppmann, L. X. Chen, and Z. Cheng, "Human serum albumin conjugated biomolecules for cancer molecular imaging," *Curr. Pharm. Des.* **18**(8), 1023–1031 (2012).
9. G. Fanali, A. D. Masi, V. Trezza, M. Marino, M. Fasano, and P. Ascenzi, "Human serum albumin: from bench to bedside," *Mol. Aspects Med.* **33**(3), 209–290 (2012).
10. X. M. He and D. C. Carter, "Atomic structure and chemistry of human serum albumin," *Nature* **358**(6383), 209–215 (1992).
11. K. Wosikowski, E. Biedermann, B. Rattel, N. Breiter, P. Jank, R. Löser, G. Jansen, and G. J. Peters, "In vitro and in vivo antitumor activity of methotrexate conjugated to human serum albumin in human cancer cells," *Clin. Cancer Res.* **9**, 1917–1926 (2003).
12. H. Thakkar, R. K. Sharma, A. K. Mishra, K. Chuttani, and R. R. Murthy, "Albumin microspheres as carriers for the antiarthritic drug celecoxib," *AAPS Pharm. Sci. Tech.* **6**(1), E65–E73 (2005).
13. Y. Bai, N. Ohno, N. Terada, S. Saitoh, T. Nakazawa, N. Nakamura, R. Katoh, and S. Ohno, "Immunolocalization of serum proteins in xenografted mouse model of human tumor cells by various cryotechniques," *Histol. Histopathol.* **24**, 717–728 (2009).
14. E. B. V. Munster and T. W. J. Gadella, "Fluorescence lifetime imaging microscopy (FLIM)," *Adv. Biochem. Eng/Biotechnol.* **95**, 143–175 (2005).
15. M. Carlson, A. L. Watson, L. Anderson, D. A. Largaespada, and P. P. Provenzano, "Multiphoton fluorescence lifetime imaging of chemotherapy distribution in solid tumors," *J. Biomed. Opt.* **22**(11), 116010 (2017).
16. A. Celli, S. Sanchez, M. Behne, T. Hazlett, E. Gratton, and T. Mauro, "The epidermal  $\text{Ca}^{2+}$  gradient: measurement using the phasor representation of fluorescent lifetime imaging," *Biophys. J.* **98**(5), 911–921 (2010).
17. T. Luo, Y. Lu, S. X. Liu, D. Y. Lin, and J. L. Qu, "Phasor-FLIM as a screening tool for the differential diagnosis of actinic keratosis, Bowen's disease, and basal cell carcinoma," *Anal. Chem.* **89**(15), 8104–8111 (2017).
18. B. Pradère, F. Poulon, E. Compérat, I. T. Lucas, D. Bazin, S. Doizi, O. Cussenot, O. Traxer, and D. A. Haidar, "Two-photon optical imaging, spectral and fluorescence lifetime analysis to discriminate urothelial carcinoma grades," *J. Biophotonics* **11**(11), e201800065 (2018).
19. S. X. You, H. H. Tu, E. J. Chaney, Y. Sun, Y. Zhao, A. J. Bower, Y. Z. Liu, M. Marjanovic, S. Sinha, Y. Pu, and S. A. Boppart, "Intravital imaging by simultaneous label-free autofluorescence-multiharmonic microscopy," *Nat. Commun.* **9**(1), 2125 (2018).
20. R. X. Yi, P. Das, F. R. Lin, B. L. Shen, Z. G. Yang, Y. H. Zhao, L. Hong, Y. He, R. Hu, J. Song, J. L. Qu, and L. W. Liu, "Fluorescence enhancement of small squaraine dye and its two-photon excited fluorescence in long-term near-infrared I&II bioimaging," *Opt. Express* **27**(9), 12360 (2019).
21. F. R. Lin, P. Das, Y. H. Zhao, B. L. Shen, R. Hu, F. F. Zhou, L. W. Liu, and J. L. Qu, "Monitoring the endocytosis of bovine serum albumin based on the fluorescence lifetime of small squaraine dye in living cells," *Biomed. Opt. Express* **11**(1), 149–159 (2020).
22. H. J. Waldvogel, M. A. Curtis, K. Baer, M. Rees, and R. L. M. Faull, "Immunohistochemical staining of post-mortem adult human brain sections," *Nat. Protoc.* **1**(6), 2719–2732 (2006).
23. Y. Q. Bai, B. Wu, N. Terada, Y. Saitoh, N. Ohno, S. Saitoh, and S. Ohno, "Immunohistochemical analysis of various serum proteins in living mouse thymus with in vivo cryotechnique," *Med. Mol. Morphol.* **45**(3), 129–139 (2012).
24. D. M. Jameson, E. Gratton, and R. D. Hall, "The measurement and analysis of heterogeneous emissions by multifrequency phase and modulation fluorometry," *Appl. Spectrosc. Rev.* **20**(1), 55–106 (1984).
25. K. Tilbury and P. J. Campagnola, "Applications of second-harmonic generation imaging microscopy in ovarian and breast cancer," *Perspect. Med. Chem.* **7**, PMC.S13214 (2015).
26. C. Stringari, A. Cinquin, O. Cinquin, M. A. Digman, P. J. Donovan, and E. Gratton, "Phasor approach to fluorescence lifetime microscopy distinguishes different metabolic states of germ cells in a live tissue," *Proc. Natl. Acad. Sci. U. S. A.* **108**(33), 13582–13587 (2011).
27. B. L. Shen, J. S. Yan, S. Q. Wang, F. F. Zhou, Y. H. Zhao, R. Hu, J. L. Qu, and L. W. Liu, "Label-free whole-colony imaging and metabolic analysis of metastatic pancreatic cancer by an autoregulating flexible optical system," *Theranostics* **10**(4), 1849–1860 (2020).

28. M. D. Barber, J. A. Ross, and K. C. H. Fearon, "Changes in nutritional, functional, and inflammatory markers in advanced pancreatic cancer," *Nutr. Cancer* **35**(2), 106–110 (1999).
29. D. C. McMillan, W. S. Watson, P. O'Gorman, T. Preston, H. R. Scott, and C. S. McArdle, "Albumin concentrations are primarily determined by the body cell mass and the systemic inflammatory response in cancer patients with weight loss," *Nutr. Cancer* **39**(2), 210–213 (2001).
30. D. Fukumura and R. K. Jain, "Tumor microvasculature and microenvironment: targets for anti-angiogenesis and normalization," *Microvasc. Res.* **74**(2-3), 72–84 (2007).
31. N. Ohno, N. Terada, Y. Bai, S. Saitoh, T. Nakazawa, N. Nakamura, I. Naito, Y. Fujii, R. Katoh, and S. Ohno, "Application of cryobiopsy to morphological and immunohistochemical analyses of xenografted human lung cancer tissues and functional blood vessels," *Cancer* **113**(5), 1068–1079 (2008).
32. R. K. Jain, "Determinants of tumor blood flow: a review," *Cancer Res.* **48**(10), 2641–2658 (1988).
33. P. A. Netti, D. A. Berk, M. A. Swartz, A. J. Grodzinsky, and R. K. Jain, "Role of extracellular matrix assembly in interstitial transport in solid tumors," *Cancer Res.* **60**(9), 2497–2503 (2000).
34. D. Tilki, N. Kilic, S. Sevinc, F. Zywiets, C. G. Stief, and S. Ergun, "Zone-specific remodeling of tumor blood vessels affects tumor growth," *Cancer* **110**(10), 2347–2362 (2007).